CsPbBr$_3$ perovskites: A dual fluorescence sensor to distinguish ethanol from methanol
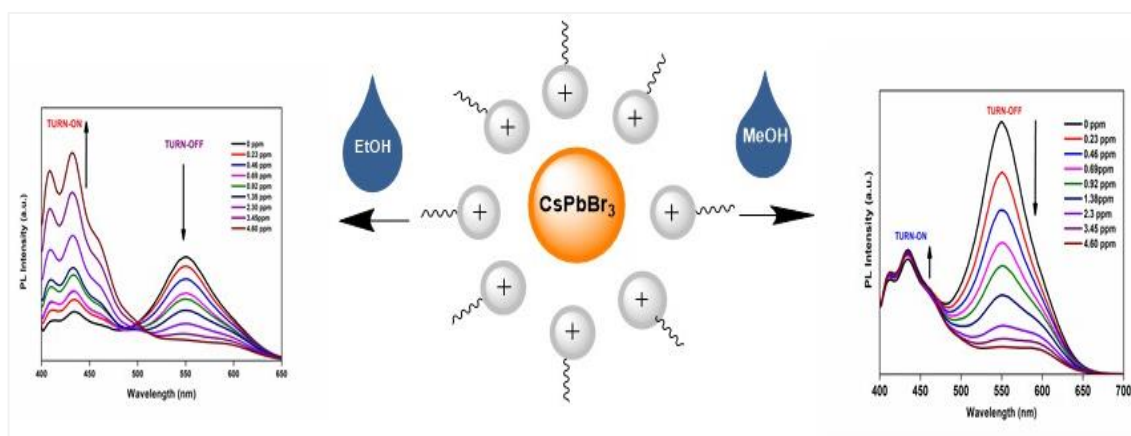
Priyankamoni Saikia, Swapan Kumar Dolui *, Sanjeev Pran Mahanta *

Department of Chemical Sciences, Tezpur University, Sonitpur 784028, Assam, India

Chapter 3

"CsPbBr$_3$ Perovskites: A dual Fluorescence sensor to distinguish ethanol from methanol"

Highlights: The chapter mentions synthesis of different passivated CsPbBr$_3$ and utilizes it for sensing of alcohols. The fascinating part of the chapter is about discussion on distinction of ethanol sensing in presence of methanol, and both alcohols show its characteristic fluorescence property with the selected perovskite.

Saikia, P., Dolui, S. K., and Mahanta, S. P. CsPbBr$_3$ Perovskites: A dual Fluorescence sensor to distinguish ethanol from methanol. *Spectrochimica Acta Part A: Molecular and Biomolecular Spectroscopy*, 291(122309):128, 2023.

Chapter 3

3.1 Introduction

Alcohols have been known for their wide application in various fields such as chemical feedstocks, bio-medical applications, and food industries [1,2]. Ethanol is one of the common ingredients in many alcoholic brews such as wine, beer, soft drinks, etc. Because of this, overconsumption of ethanol could lead to many health issues (nausea, cancer, headache), and in addition, incidents like motor vehicle crashes, and crimes are most seen. World Health Organization (WHO) declares that approximately 2.5 million people death occurs every year due to the harmful effects of alcohol [3]. Apart from its negative impacts, ethanol is considered a renewable fuel and ethanol blending in petrol has been adopted by many countries to reduce pollution [4]. Like ethanol, methanol poisoning can cause blindness, organ failure, or even death when it is recognized too late [5-8]. Due to the drinking of methanol-containing adulterated wine, many methanol-poisoning incidents occur every year. As these compounds are an important part of human life, it is an urgent need to develop high selectivity, sensitivity sensors for the detection of alcohol.

In that context, traditionally spectrophotometric methods, optical methods [9], electrical resistance response methods [10], chromatographic [11,12], and mass spectroscopic[13,14], etc. are widely explored for the determination of alcohol in liquid samples. Additionally, it is of great importance to the selective detection of ethanol over methanol and other alcohols [15-17]. Chemo-sensors provide simple and easy detection techniques for the analytes [18-22]. Therefore, to design of a chemo-sensor to determine the presence of alcohol and ascertain the nature of alcohol in a sample is of paramount interest.

In the last few years, researchers investigated perovskites as a great potential candidate for chemo-sensors development towards different analytes (metals, biomolecules, toxic molecules) in solution as well as in the gas phase [23,24]. $CsPbBr_3$ has shown its wide applications in optoelectronics devices, and sensor development due to its facile solution processable synthesis and defect-sensitive optoelectronic properties [25-32]. In that context, Lu et al. used $CsPbX_3$ (X = Cl, Br, I) quantum dots to detect mercury ions [33]. Similarly, Zhang et al. [34] used $CsPbBr_3$ as a colorimetric fluorescence sensing probe to detect Pb^{2+} ions. Lu et al. encapsulated $CH_3NHPbBr_3$ with ligand *n*-octylamine and 6-amino-1-hexanol for

fluoride detection [35]. These studies have greatly encouraged the development of lead halide perovskites as a sensing probe.

Surfactants are being used as a surface and bulk passivator in the perovskite particles to improve the luminescence and chemical stability properties [36,37]. The hydrophobic tail component can stimulate the surface stability of the perovskites from the polar environment. Thus, it stabilizes the uncoordinated halide ions and lessens the surface defects.

In this chapter, *in-situ* passivation of CsPbBr$_3$ metal halide perovskites (MHP) with different kinds of surfactants like cationic (cetyltrimethylammonium ammonium bromide, CTAB), anionic (sodium dodecyl benzene sulfonate, SDBS), and non-ionic (triton x-100, TX-100) as a surface ligand was studied. The impact of different passivation on the chemical stability of CsPbBr$_3$ has been investigated. Among them, the most stable CTAB@CsPbBr$_3$ was designed to develop a dual ratio-metric fluorescence sensor towards alcohols. It is found that CsPbBr$_3$ and CTAB@CsPbBr$_3$ can selectively sense alcohols and can be able to successfully differentiate ethanol from methanol effectively.

3.2 Experimental

3.2.1 Materials

All used chemicals were purchased from available suppliers and utilized without purification. Cesium Bromide (CsBr, 99.9%, Alfa Aesar), Lead Bromide (PbBr$_2$, 98%, Sigma Aldrich), Dimethyl Sulfoxide (DMSO) (99%, SRL), Sodium Dodecyl Benzene Sulfonate (SDBS, Sigma Aldrich), Cetyl Trimethyl Ammonium Bromide (CTAB, Rankem), Triton X-100 (TX-100, Sigma Aldrich), Toluene (Sigma Aldrich), Ethanol (99%, Alfa-Aesar), Tetrahydrofuran (THF) (Alfa-Aesar), 1,4-dioxane (Alfa-Aesar), Isopropanol (Alfa-Aesar), Acetone (Rankem), Diethyl ether (Alfa-Aesar), Hexane (Alfa-Aesar), Methanol (Alfa-Aesar), *tert*-butyl alcohol (Alfa-Aesar), Dimethylformamide (DMF) (Alfa-Aesar), Dimethyl acetamide (Alfa-Aesar), Ethyl acetate (Alfa-Aesar), Cough-syrup (Gulfadryl, Galpha) were commercially available.

3.2.2 Synthesis of different cationic, anionic, and non-ionic surfactant passivated CsPbBr$_3$

The different ionic and non-ionic surfactant passivated CsPbBr$_3$ (MHPs) were synthesized using a one-pot synthesis method. For the synthesis of passivated

perovskites, 2.5 mmol of CsBr, 2 mmol of $PbBr_2$, and 0.2 mmol of differently charged surfactants (CTAB, SDBS, TX-100) were dissolved in 15 mL DMSO and stirred for 12 hours to form a clear precursor solution. For crystallization, the above 15 mL solution was poured into 150 mL toluene under vigorous stirring. Then, the passivated $CsPbBr_3$ (MHPs) crystals were collected by centrifugation and dried in a vacuum oven at 80 ℃ for overnight [38].

3.2.3 Structural Characterization

FT-IR spectra of the prepared samples were performed using Nicolet Impact-410 IR spectrometer (USA) in the KBr medium at room temperature in the range of 4000–400 cm^{-1}. XRD was measured with Rigaku Miniflex X-ray diffractometer (Tokyo, Japan) with Cu Kα radiation (δ = 0.15418 nm, scanning rate = 0.05 s^{-1}) at 30 kV and 15 mA in a 2θ range of 7° to 80°. The surface morphologies of $CsPbBr_3$ MHPs were analysed by using SEM (JEOL-JSM-6390LV). Energy Dispersive X-Ray Analysis (EDX) analysis was also measured by SEM (JEOL-JSM-6390LV) attached to SEM. The Transmission electron microscope was recorded on (Model: JEM-2100, JEOL, USA). X-ray photoelectron spectroscopy (XPS) spectra were recorded with an ESCALAB 220 XL spectrometer from Vacuum Generators featuring a monochromatic Al Kα X-ray source (1486.6 eV) and a spherical energy analyser operated in the CAE (constant analyser energy) mode (CAE = 100 eV for survey spectra and CAE = 40 eV for high-resolution spectra), using the electromagnetic lens mode. A Shimadzu UV-2550 spectrophotometer was used to record the electronic absorption spectra of the samples in the wavelength range of 200-800 nm. Photoluminescence spectra were recorded using a Hitachi F-2700 fluorescence spectrophotometer at room temperature. Time-resolved PL (TRPL) measurement data were acquired by using a 310 nm pulse laser excitation with an instrument response of 10 ps (Life Spec II, Edinburg Instrument).

3.2.4 Fluorescence measurements

To measure the photoluminescence (PL) properties, $CsPbBr_3$ precipitate (0.32 mg) were dissolved in 10 mL DMF and stirred for 2 hours to form a clear solution. The photostability test was performed where the solution was exposed to the illumination of UV light (365 nm) for 8 hours. Later, to study the effect of polar solvents a stability test was performed by adding different polar solvents to the

perovskite solution and monitored the PL up to 70 min. The PL emission spectra of the samples were tested within an interval every 10 min.

The sensing study was performed by adding known quantity of the analyte liquid to the perovskite solution. The fluorescence spectra were measured after addition of different amount of analyte solvent in a 3 mL perovskite solution in DMF. After the incubation period of 10 min, the luminescence intensity values of the respective solution were measured under the single excitation wavelength of 310 nm. The quenching efficiency was calculated by using the Stern-Volmer equation [39].

$$\frac{I_0}{I} = 1 + \text{Ksv[C]}$$

In this equation, I_0 is the initial luminescence intensity of the perovskite solution without the addition of alcohol, and I is the luminescence intensity of the perovskite solution with the addition of analyte alcohols. K_{sv} is the Stern-Volmer quenching constant, and C is the concentration of the quencher. The relationship between alcohol concentration and PL intensity can be linearly fitted and from slope of the equation, the Stern-Volmer constant (K_{sv}) is calculated.

3.2.4.1 Photoluminescence Quantum Yield (PLQY) measurement

The Photoluminescence Quantum Yield (PLQY) of the different ionic and non-ionic passivated perovskites was measured by using Rhodamine Blue as a reference (Quantum yield = 97% in ethanol) [40-42]. The PLQY was calculated using the following equation [40].

$$\Phi_{\text{fx}} = \frac{\eta_x^2}{\eta_{Rhodamine\ Blue}^2} \cdot \frac{A_{Rhodamine\ Blue}}{A_x} \cdot \frac{F_x}{F_{Rhodamine\ Blue}} \cdot \Phi_{fRhodamine\ Blue}$$

In the above equation, η is the refractivity (η = 1.36 for ethanol and η= 1.43 for DMF), A is the absorbance which is lower than 0.01 to avoid internal filter effects [40] and F is the integral absorption area in the respective luminescence spectra of the passivated solution.

3.2.4.2 Association constant measurement

To calculate the association constant, the intensity of the emission peak at 550 nm was considered. The following Benesi-Hildebrand equation was applied [43].

$$\frac{1}{F - F_0} = \frac{1}{\{Ka \times (Fmax - F_0) \times [alcohol]\}} + \frac{1}{F_{max} - F_0}$$

In the above equation, F_0 is the initial fluorescence intensity without the addition of alcohol and F is the fluorescence intensity after the addition of different amount of alcohol. The association constant was calculated by plotting against $[F - F_0]^{-1}$ against $[alcohol]^{-1}$. The found data are linearly fitted, and the K_a values are evaluated from the slope of the respective linear plot.

3.3 Results and Discussion

3.3.1 Structural Analysis

3.3.1.1 FT-IR analysis

FT-IR spectrum was recorded to analyse the different functional groups presence on the different ionic and non-ionic charged surfactant passivated $CsPbBr_3$ (Figure 3.1). The band at 2915 and 2848 cm^{-1} are corresponding to the asymmetric and symmetric stretching modes of C-H [44,45]. The broad absorption peak at 3437 cm^{-1} indicates the presence of absorbed H_2O molecules [45]. The peaks at 952 and 1396 cm^{-1} are corresponding to the bending vibrations of the C-H bond [46,47]. The FT-IR spectra of SDBS@$CsPbBr_3$ exhibits two bands at 608 and 1121 cm^{-1} which are responsible due to the stretching vibration of S=O [48]. The peak at 709 cm^{-1} is due to the phenyl group of SDBS [47] and the band at 1313 cm^{-1} is for the wagging mode of methylene group i.e., CH_2 [49]. The FT-IR spectra of CTAB@$CsPbBr_3$ exhibit two characteristic peaks approximately at 908 and 1470 cm^{-1} which are attributed to the stretching modes of C-N indicating the existence of CTAB [50,51]. The coordination of the surfactant Triton X-100 with $CsPbBr_3$ was confirmed by the presence of an absorption band at 1318 cm^{-1} due to the stretching mode of C-O-C [52].
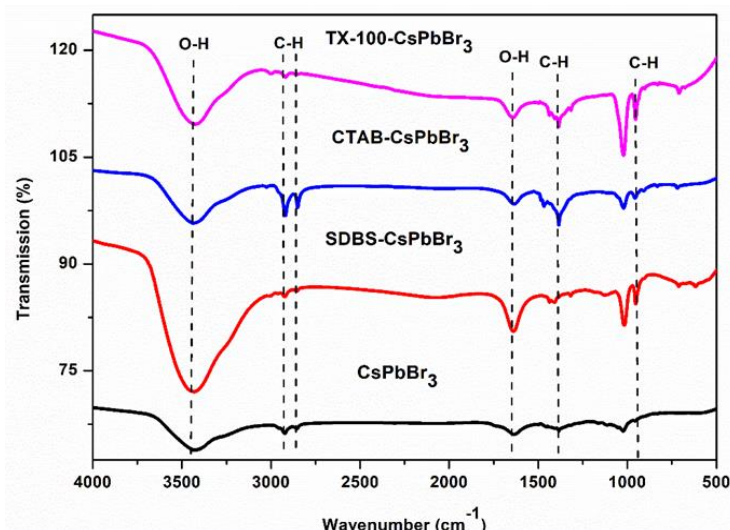
Figure 3.1 FT-IR spectra of pristine and different surfactant passivated CsPbBr$_3$ crystals

3.3.1.2 XRD analysis

The X-ray diffraction (XRD) pattern of pristine and passivated CsPbBr$_3$ was recorded (Figure 3.2). The diffraction peaks (110), (112), and (220) indexed at 15.19, 21.48, and 30.58 agrees well with the standard orthorhombic phase of perovskite crystal structure [53]. Upon passivation, the intactness of the perovskite crystal structure is confirmed from XRD analysis.
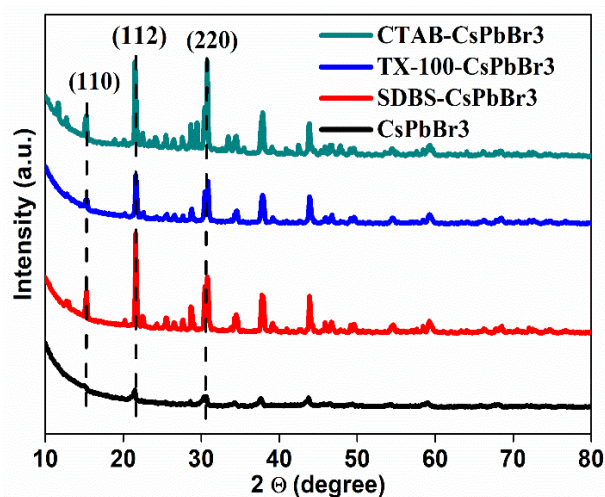

Figure 3.2 XRD spectra of pristine and different surfactant passivated CsPbBr$_3$ crystals

3.3.1.3 Optical analysis

The optical properties of the surfactant passivated CsPbBr$_3$ were studied (Figure 3.3). As it was observed, the UV-Vis absorption spectrum of pristine and passivated

perovskites exhibits a similar absorbance behaviour at 310 nm in DMF solution. Upon excitation of wavelength of 310 nm, the solutions phase photoluminescence spectra of perovskites showed broad emission at 500-600 nm with a variation in intensity. The order of the luminescence intensity is found as SDBS-CsPbBr$_3$ > CTAB-CsPbBr$_3$ > CsPbBr$_3$ > TX-100-CsPbBr$_3$ (Figure 3.4)**.** The calculated photoluminescence quantum yield of CTAB passivated CsPbBr$_3$ was found as 71%. However, the value for SDBS passivated and TX-100 passivated CsPbBr$_3$ was found as 39.28% and 51.89%. The complete luminescence results were shown in (Table 3.1). The full-width half maxima for the luminescence peaks were also calculated which was found for SDBS@CsPbBr$_3$ as 27.59 nm and for CTAB@CsPbBr$_3$ and TX-100@CsPbBr$_3$ was found as 14.34 nm and 14.20 nm, respectively. The relatively high quantum yield of CTAB passivated CsPbBr$_3$ project it as a better probe towards sensor development.
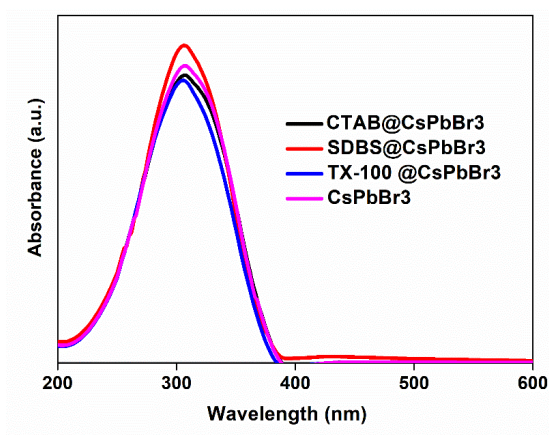
Figure 3.3 UV-Vis spectra of the different passivated CsPbBr$_3$ in DMF solution
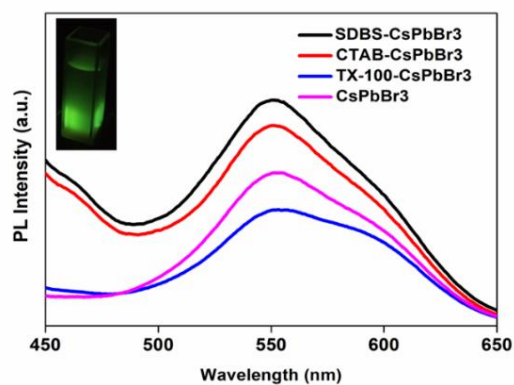
Figure 3.4 PL spectra of different passivated CsPbBr$_3$ in DMF solution upon excitation with 310 nm light (The image shows the colour of perovskite solution under the illumination of 365 nm UV-lamp)

Table 3.1 Summary of luminescence results of different passivated CsPbBr$_3$

Perovskite Sample	Surfactant	λ_{max} (nm)	FWHM (nm)	PLQY (%)
CsPbBr$_3$-SDBS	SDBS	551.5	27.59	39.28
CsPbBr$_3$-CTAB	CTAB	550.	14.34	71
CsPbBr$_3$-TX-100	TX-100	553.5	14.20	51.89

### 3.3.1.4 Energy Dispersive X-ray Analysis (EDX) analysis

To reveal the elemental information of passivated CsPbBr$_3$, EDX measurements was carried out. As depicted in Figure 3.5, the elemental ratios of EDX measurements were in close approximations with the structural compositions.
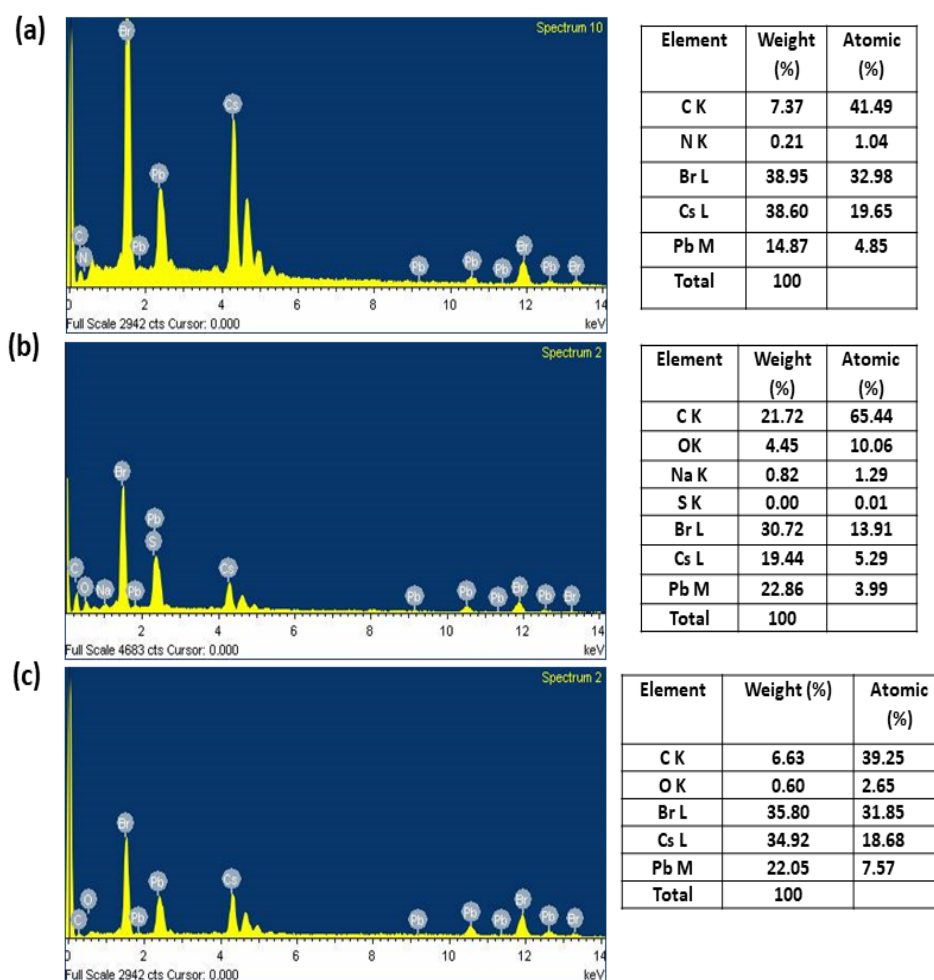
Figure 3.5 EDX spectra of (a) CTAB@CsPbBr$_3$, (b) SDBS@CsPbBr$_3$, and (c) TX-100@CsPbBr$_3$

3.3.1.5 X-ray Photoelectron spectroscopy (XPS) analysis

The high-resolution X-ray Photoelectron spectroscopy (XPS) of CTAB@CsPbBr$_3$ depicted that the CTAB successfully passivated into the perovskite CsPbBr$_3$ crystal lattice. The binding energy appeared at 738 eV and 724 eV are corresponding to Cs 3d$_{3/2}$ and Cs 3d$_{5/2}$, respectively (Figure 3.6a). The binding energies of Pb 4f $_{5/2}$ and Pb 4f $_{7/2}$ were found at 143.2 eV and 138.2 eV, respectively (Figure 3.6b). The Br3d peak is deconvoluted into two sub-peaks with binding energies appeared at 68.7 eV and 67.7 eV corresponding to Br 3d$_{5/2}$ and Br 3d$_{3/2}$ (Figure 3.6c). Also, the peak at 402.2 eV and 284.6 ev is due to the incorporated N 1s and C 1s of CTAB in the perovskite lattice (Figure 3.6d-e).
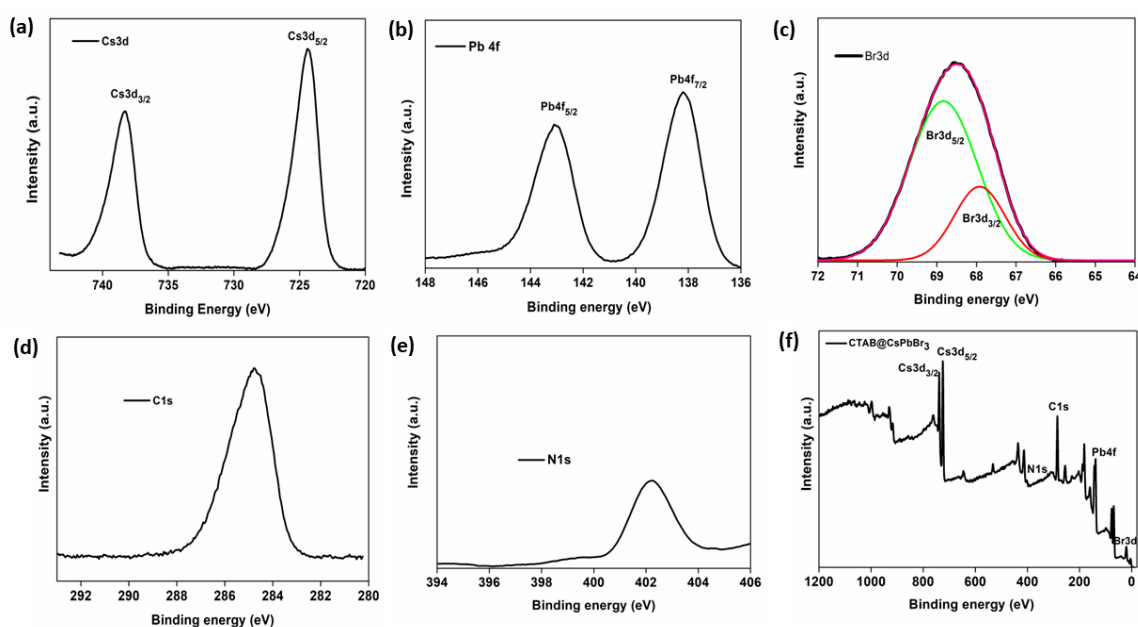

Figure 3.6 XPS survey of (a) Cs 3d spectrum. (b) Pb 4f spectrum. (c) Br 3d spectrum (d) C 1s spectrum. (e) N 1s spectrum. (f) prepared CTAB@CsPbBr$_3$ spectrum

3.3.2. Morphological analysis

3.3.2.1 SEM analysis

The SEM images for all ionic and non-ionic passivated perovskite crystal lattice indicate the formation of macro sizes particles ($\sim$ 2.5-3.0 μm) (Figure 3.7). However, the SEM image of CTAB passivated CsPbBr$_3$ reveals some aggregation of particles. This is attributed due to the influence of the bromide content of CTAB and subsequently, influence the growth kinetics assisting flocculation during CTAB passivation (average particle size $\sim$ 3.07 μm). Due to non-ionic steric repulsions, TX-

100 restricts the growth of CsPbBr$_3$ microcrystals resulting in average particle size of 2.62 μm. Also, during SDBS passivation the average particle size was found as 2.80 μm.
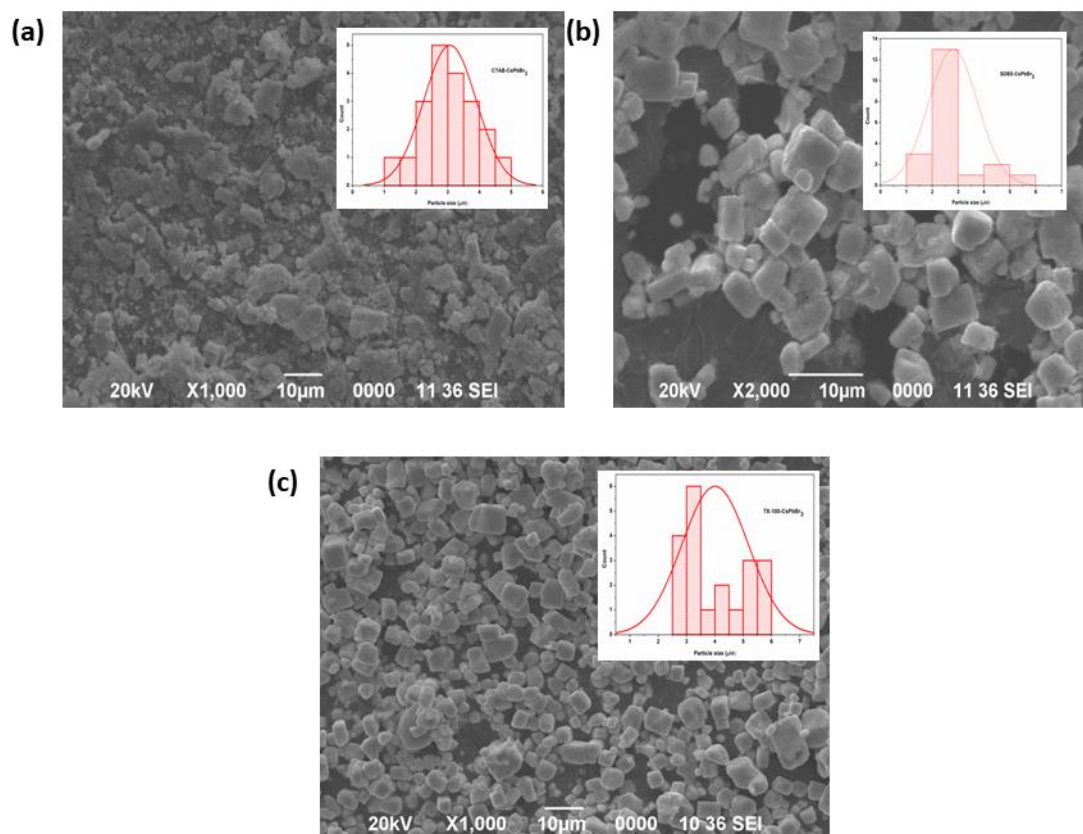
Figure 3.7 SEM images of (a) CTAB@CsPbBr$_3$ (b) SDBS@CsPbBr$_3$, and (c) TX-100@CsPbBr$_3$ along with their corresponding size statistical histogram images inset

3.3.2.2 TEM analysis

The morphology and the size of CTAB@CsPbBr$_3$ were further characterized by TEM analysis. As shown in Figure 3.8a-b, the TEM image of CsPbBr$_3$ exhibits to an orthorhombic-shaped structure. However, a rod-shaped structure is obseved in case of CTAB@CsPbBr$_3$. The selected area diffraction pattern (SAED) of the samples (Figure 3.8c-d) displayed lattice fringes of 2.2 Å and 4.2 Å are corresponding to the (110) and (220) planes of CsPbBr$_3$ and CTAB@CsPbBr$_3$ [54].
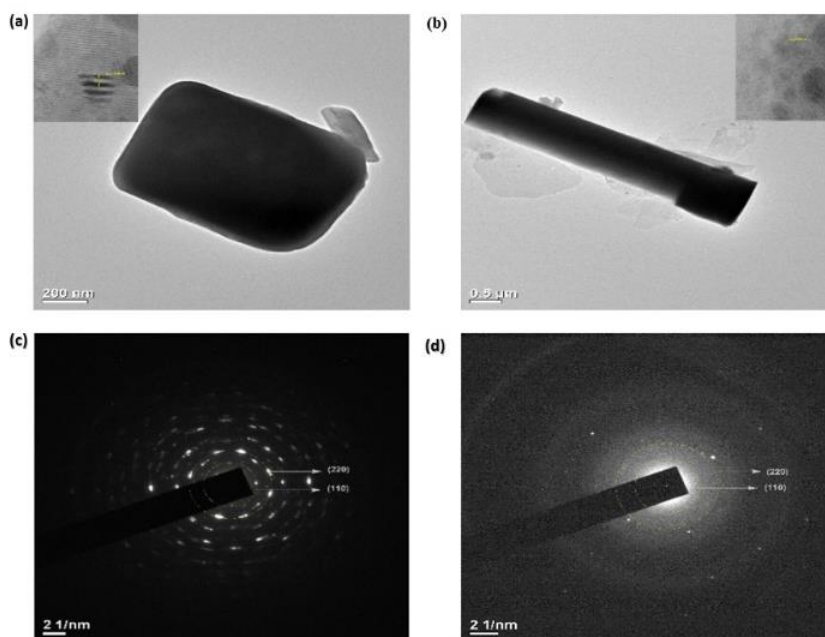
Figure 3.8 TEM images of (a) CsPbBr$_3$ (b)CsPbBr$_3$@CTAB with the interplanar distances of lattice fringes are shown in the inset and (c-d) selected area diffraction (SAED) images of CsPbBr$_3$ and CsPbBr$_3$@CTAB
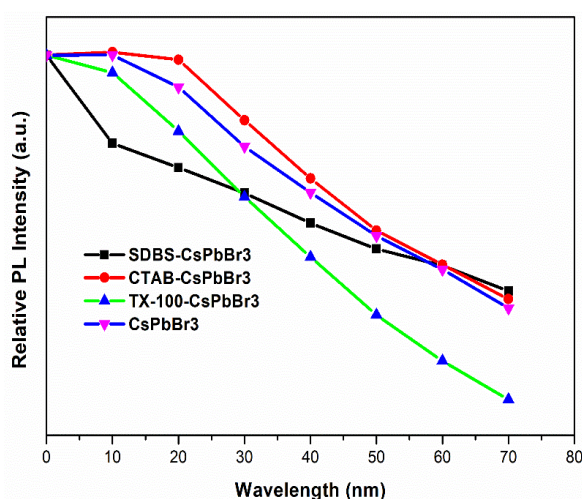
3.3.3 Study of stability of different passivated CsPbBr$_3$

A stability test was performed with the addition of 100 µL of water to 3 mL DMF solution of the passivated CsPbBr$_3$. The subsequent fluorescent intensity was measured at different intervals of time. The luminescence, intensity of the synthesized materials gradually decreases with time. This result can be understood because of the degradation of CsPbBr$_3$ by H$_2$O. The calculated percentage of degradation of CTAB@CsPbBr$_3$ was found to be 10.59%, whereas SDBS@CsPbBr$_3$ and TX-100@CsPbBr$_3$ showed the values 13.05 % and 19.52 % respectively within 70 mins (Figure 3.9). The less percentage of degradation of CTAB@CsPbBr$_3$ is attributed to the reason that the cationic nature of CTAB enables the relatively stronger attachment to the CsPbBr$_3$ surface and the bromide precursor makes the perovskite stable towards humid conditions. However, the SDBS@CsPbBr$_3$ solution also displays negligible degradation under humid conditions for 30 min. After 30 min, it showed a sharp decay in the PL intensity. The results may be due to the formation of a compact SDBS bilayer due to the π-π interaction of the phenyl moieties that initially slows down the diffusion of the water molecules to the perovskite surface. TX-100, makes less passivation to the perovskite structure due to the steric hindrance of the non-ionic branched structure of the surfactant.
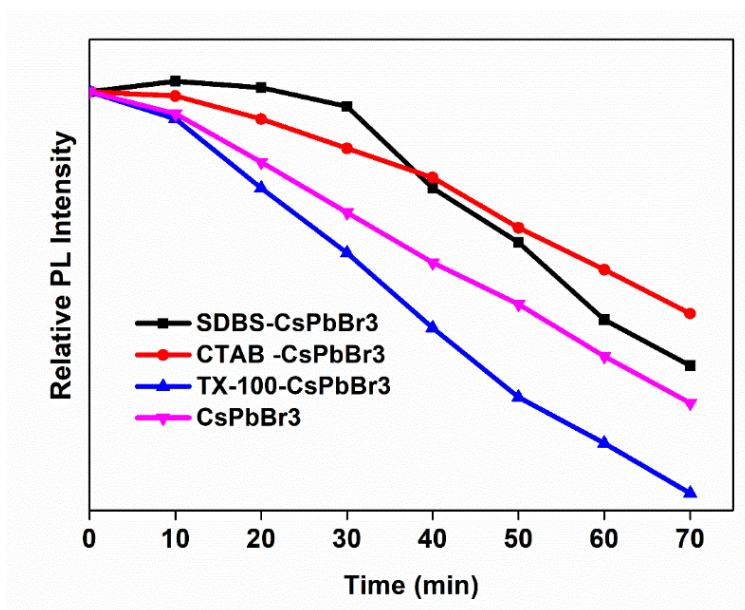
**Figure 3.9** Decay PL intensity of CsPbBr$_3$ with time upon addition of water

It is observed that the addition of alcohols showed quenching of the fluorescence signal of CsPbBr$_3$ (CsPbBr$_3$, CTAB@CsPbBr$_3$, and SDBS@CsPbBr$_3$) perovskite at 550 nm (Figure 3.10). However, with the addition of alcohols to TX-100@CsPbBr$_3$ solution some degradations were noticed which is attributed due to its non-ionic interaction. However, CTAB@CsPbBr$_3$ was selected for the alcohol sensing study owing to its relatively higher aqueous stability.

Figure 3.10 Change in the PL spectra of different passivated CsPbBr$_3$ with the addition of ethanol

The photostability of the passivated perovskites was performed by irradiating the passivated CsPbBr$_3$ perovskites under the illumination of a 365 nm wavelength UV

lamp for a period of 8 hours by keeping the light source 12 cm away from the sample to avoid the possibility of thermal degradation. The calculated normalized PL intensity ratio before and after irradiation for pristine $CsPbBr_3$, $SDBS@CsPbBr_3$. $CTAB@CsPbBr$, and $TX-100@CsPbBr_3$ were 54.3%, 55.4%, 55.7%, and 49.46% respectively (Figure 3.11). This observation depicts that surfactant passivation might not influence photostability of $CsPbBr_3$.
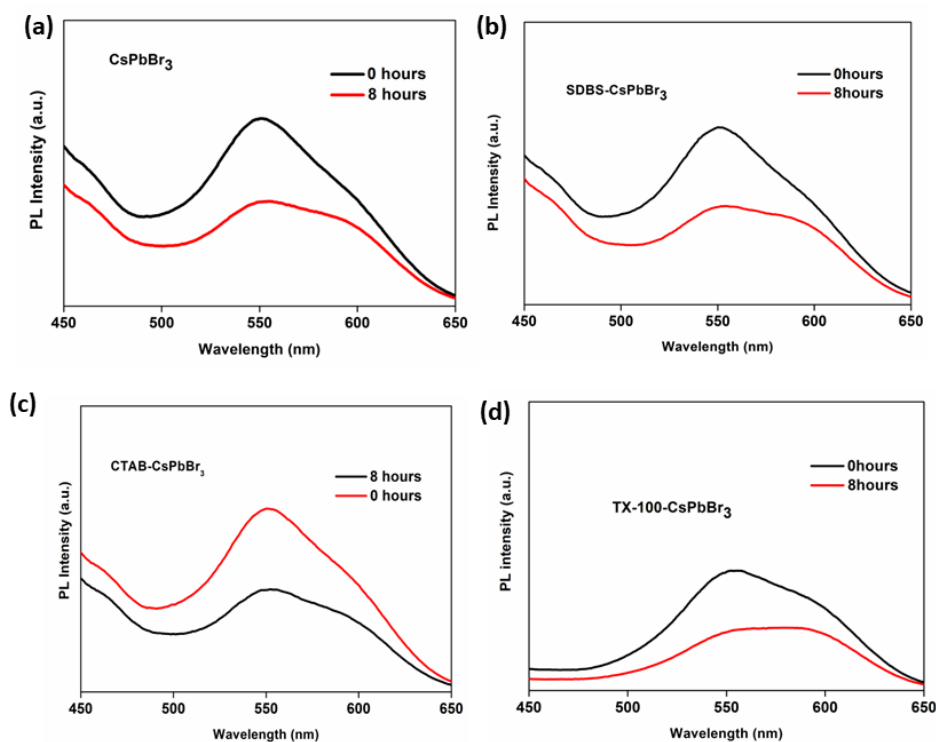

Figure 3.11 Decay PL graph of (a) $CsPbBr_3$, (b) $SDBS@CsPbBr_3$, (c) $CTAB@CsPbBr_3$, and (d) $TX-100@CsPbBr_3$ exposure to UV-irradiation reflecting the photostability of the passivated $CsPbBr_3$

### 3.3.4 Solvent sensing behaviour of CTAB passivated $CsPbBr_3$

To investigate the chemical stability of $CTAB@CsPbBr_3$ some commonly used laboratory solvents like THF, 1,4-dioxane, acetone, diethyl ether, hexane, 2-methyl tetrahydrofuran, dimethylacetamide, ethyl acetate and alcohols such as ethanol, methanol, *tert*-butyl alcohol, and isopropanol were considered. A stock solution of perovskite (0.1 mmol) in 10 mL DMF is prepared and from that solution an aliquot of 3 mL was taken to carry out the luminescence measurements. All emission spectra were recorded under the excitation wavelength of 310 nm. The fluroscence of the

CTAB@CsPbBr$_3$ solution was measured by adding 100 μL of the solvent chosen for study. In this study, it was noticed that with the addition of common laboratory solvents, there was no any noticeable quenching of the emission peak at 550 nm (Figure 3.12). However, with the addition of alcohols the emission peak of perovskite quenches (Figure 3.13).
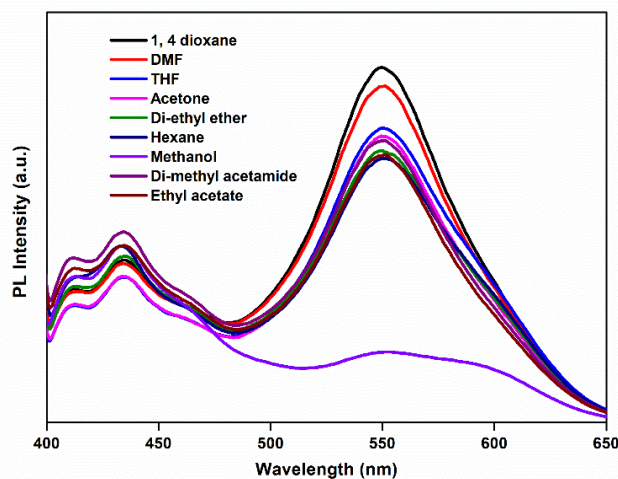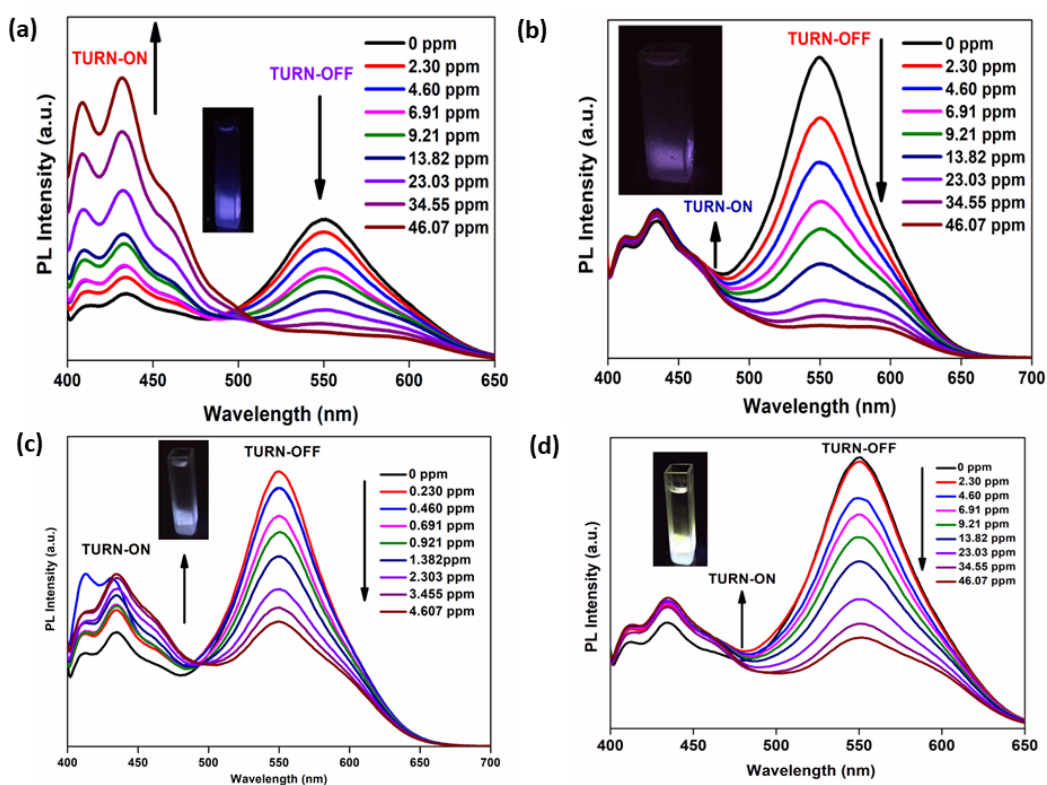

Figure 3.12 Change in the PL spectra of CTAB@CsPbBr$_3$ with the addition of non-alcoholic solvent
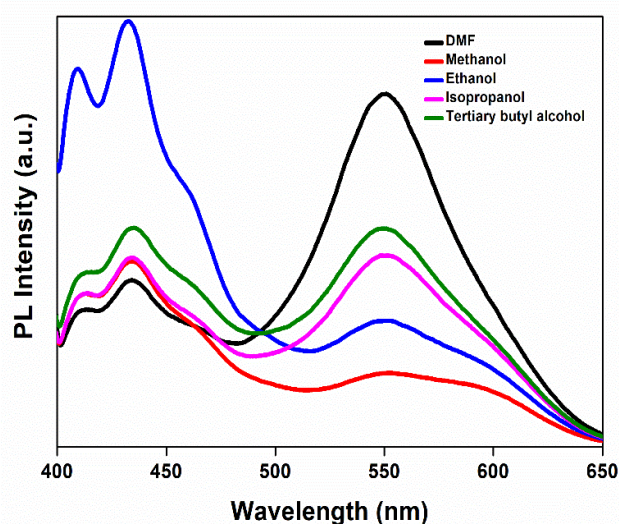
Figure 3.13 Change in the PL spectra of CTAB@CsPbBr$_3$ with the addition of alcoholic solvent

In figure 3.14(a), it was noticed that the titration of CTAB@CsPbBr$_3$ solution with ethanol showed gradual fluorescence turn-off at 550 nm and turn-on at 430 nm with maintaining an isosbestic point at 490 nm. The calculated (I_{430}/I_{550}) value showed a

linear increase with the increase in the concentration of ethanol to CTAB@CsPbBr$_3$ in DMF which provides dual ratiometric behaviour. In the PL spectra (Figure 3.14), it is quite remarkable obsrvation that with the addition of other alcohol, the emission peak at 550 nm gradually decreases. But in the presence of ethanol, only the emergence of the peak at 430 nm occurs. Because of this charcteristic behavior in PL study, the sensing method can be applicable to distinguish ethanol from other alcohols owing to its different modes of interaction.

Figure 3.14 Change in the PL spectra of CTAB@CsPbBr$_3$ with the addition of (a) ethanol, (b) methanol, (c) *tert*-butyl alcohol, and (d) isopropanol
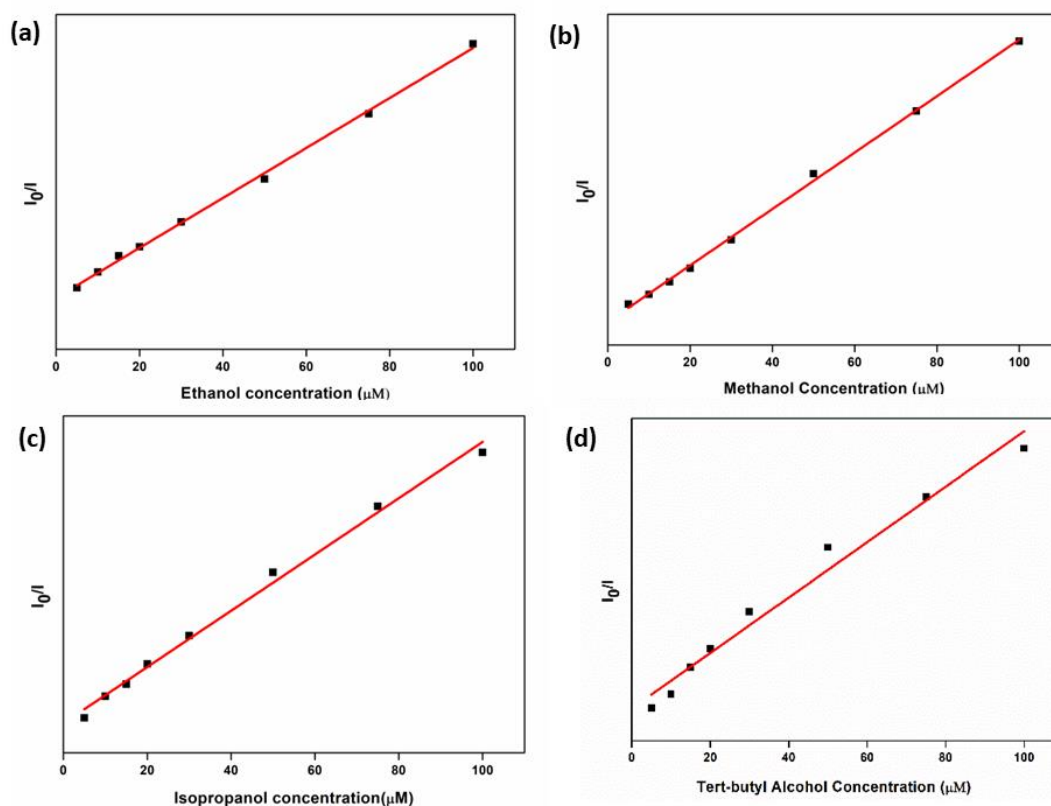
Stern-Volmer constant [39] was calculated from the titration data of CTAB@CsPbBr$_3$ solution with different alcohols considered for the study and the results were found as 4×10^4, 8.5×10^4, 2×10^4, and 1.2×10^4 M^{-1} for ethanol, methanol, isopropanol, and *tert*-butyl alcohol, respectively (Figure 3.15). The similar Stern-Volmer constant value indicates almost similar kinetics of quenching for all the studied alcohols due to their similar nature of interaction with the excited state.

Later, using the Benesi-Hildebrand method, the association constant of the alcohols to the CTAB @ CsPbBr$_3$ was calculated from the quenching data and obtained almost similar binding constants such as 6.18×10^4 and 2.3×10^4 M^{-1} for ethanol, and

methanol, respectively. The complete data of sensing experiments are tabulated in following tables (Table 3.2 and 3.3).

Figure 3.15 Stern-Volmer plots of CTAB@CsPbBr$_3$ towards (a) ethanol, (b) methanol, (c) isopropanol, and (d) *tert*-butyl alcohol

**Table 3.2** Summary of Stern–Volmer constant (K$_{SV}$) calculated from the titration data

Analytes	Slope (KµM^{-1})	RSD (R^2)	Detection limit(3σ/K) (µM)	Detection Limit (ppb)
Ethanol	0.040	0.99	0.160	7.37
Methanol	0.085	0.99	0.141	6.53
Isopropanol	0.020	0.99	0.286	13.18
tert-butyl alcohol	0.012	0.97	0.568	26.17

Table 3.3 Summary of association constant (K_a) of the alcohols to the CTAB@CsPbBr$_3$

| Analytes	Association constant (K_a)	r^2 values
Ethanol	6.18×10^4 M^{-1}	0.96
Methanol	2.18×10^4 M^{-1}	0.99
tert-butyl alcohol	4.53×10^6 M^{-1}	0.55
Isopropanol	35.20×10^4 M^{-1}	0.81

Interestingly, in contrast to other alcohols, with the addition of ethanol emergences a new broad doublet at 413 nm and 430 nm (Figure. 3.14a). From this observation, we can able to conclude that the broad peak at 550 nm can be used to sense the alcohols from other laboratory-used solvents and the peak at 410-470 nm can be used to discriminate ethanol from other alcohols. In addition, the chemoselective behaviour of the designed sensor was also investigated. The designed sensor CTAB@CsPbBr$_3$ solution was first exposed with 3.2 ppm of methanol and then gradually added ethanol and vice versa, and concomitantly the fluorescence spectra of the respective titrations are monitored (Figure 3.16a). Upon the addition of methanol, complete quenching of the 550 nm signal was observed followed by the emergence of the peak at 430 nm upon the addition of ethanol. This observation unequivocally confirmed the chemoselective nature of CTAB@CsPbBr$_3$ between ethanol and methanol (Figure 3.16b). The limit of detection calculated from the calibration curve fitting was 7.3 ppb for ethanol.
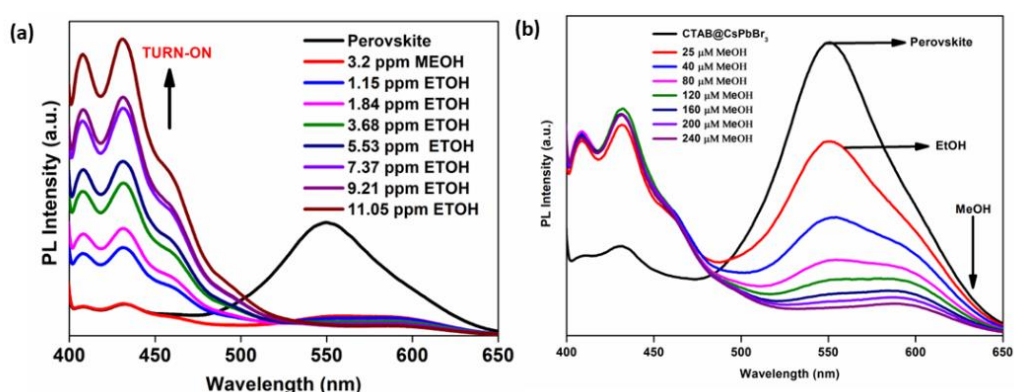

Figure 3.16 Fluorescence turn-on of CTAB@CsPbBr$_3$ (a) methanol solution upon gradual addition of ethanol (b) ethanol solution upon gradual addition of methanol solution

The vapor sensing potential of the CTAB@CsPbBr$_3$ perovskite is further explored. Upon exposure of solid CTAB@CsPbBr$_3$ crystals to ethanol vapor. Significant quenching of CTAB@CsPbBr$_3$ at 550 nm emission is noticed (Figure 3.17 a and Figure 3.18). Unlike the solution phase, the turn-on response at 430 nm is not observed when ethanol vapor is exposed to the perovskite surface owing to the relatively lower concentration of the ethanol vapor available to reaction with the surface and eventually slower rate of degradation. Also, the absorbance spectra of CTAB@CsPbBr$_3$ upon exposure to alcohol were investigated. Lower absorbance intensity was noticed when ethanol vapor exposed (Figure 3.17b).
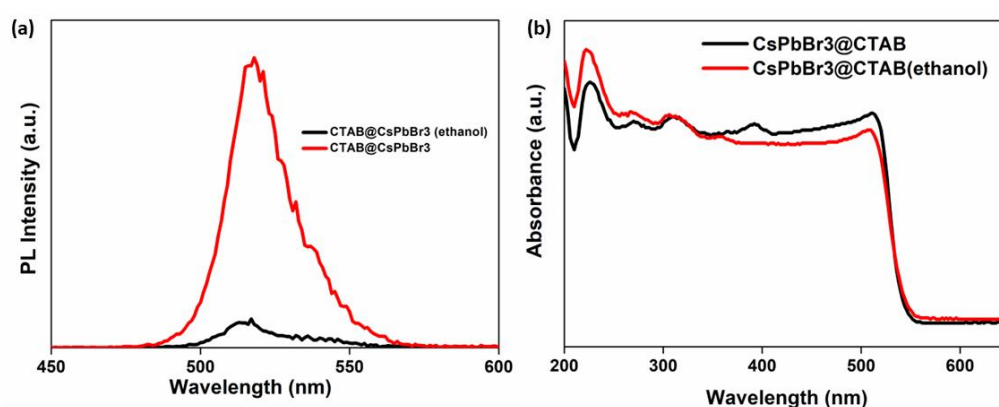

Figure 3.17 (a) Solid-state PL spectra of CTAB@CsPbBr$_3$ before and after alcohol exposure, (b) solid-state UV-Vis spectra of CTAB@CsPbBr$_3$ before and after alcohol exposure
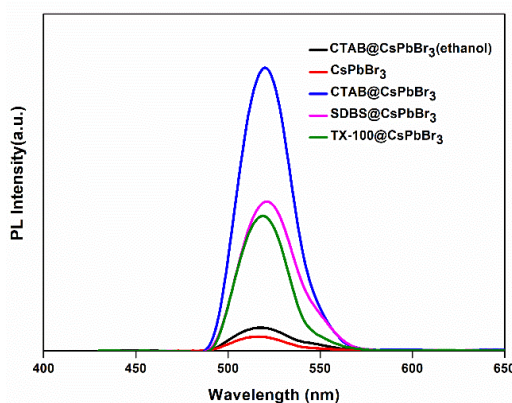
Figure 3.18 Solid-state luminescence spectra of pristine and different passivated CsPbBr$_3$ before and after exposure to alcohols with the excitation wavelength of 310 nm

3.3.5 Selective sensing of passivated CsPbBr₃

To study the selectivity of the CTAB@CsPbBr₃ towards alcohol detection, several common solvents were used in the laboratory (THF, 1,4-dioxane, acetic acid, acetone, diethyl ether, hexane, 2-Methyltetrahydroxy furan, dimethylacetamide, and ethyl-acetate) were selected as interfering analyte (Figure 3.19a). As depicted in Figure 3.19a, the CTAB@CsPbBr₃ shows selectivity towards the tested alcohols with a significant decrease in intensity. However, the peak at 430 nm showed a remarkable enhancement of the peak intensity upon the addition of ethanol (Figure 3.19b). The results demonstrated CTAB@CsPbBr₃ as a new fluorescence sensor for alcohol detection with good selectivity.
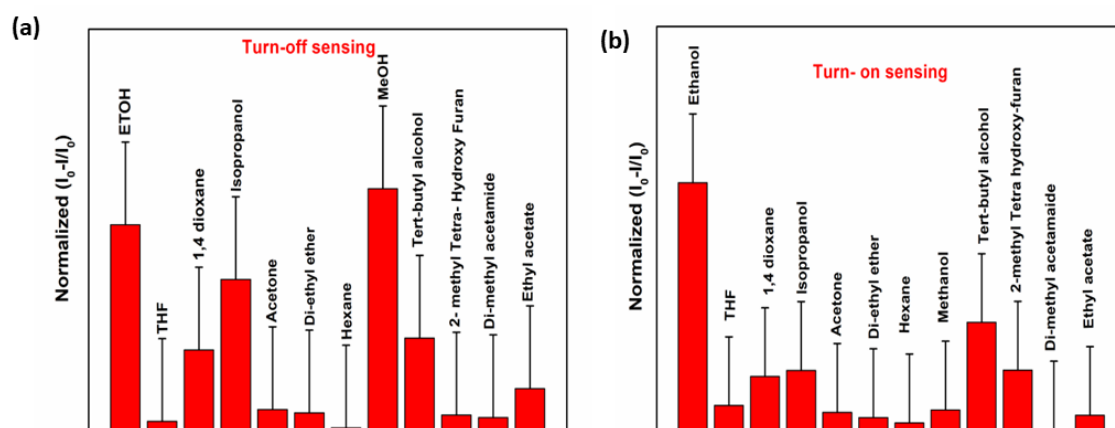

Figure 3.19 Selectivity of CTAB@CsPbBr₃ (a) w.r.t. turn off response at 550 nm in the presence of competing studied solvents, and (b) w.r.t. turn on the response at 430 nm upon addition of an excess of the studied widely used laboratory solvents

3.3.6 Sensing mechanism of passivated CsPbBr₃ towards alcohols

The quenching mechanism of CTAB@CsPbBr₃ towards alcohols was further investigated. The absorption spectra of the CTAB@CsPbBr₃ in DMF solution in the absence and presence of alcohols were compared. The possibility of pure static quenching owing to the absence of any perturbations of CTAB@CsPbBr₃ absorption was featured upon alcohol addition (Figure 3.20a). The TRPL spectra of CTAB@CsPbBr₃ in the presence and absence of alcohols were recorded with an excitation wavelength of 310 nm (Figure 3.20b). The decay curves at the wavelength 550 nm were well fitted in the bi-exponential decay fit model. The calculated average lifetime of the excited state of CTAB@CsPbBr₃ was found as 0.37 ns, while in the

presence of alcohol, the lifetime of the excited state of CTAB@CsPbBr$_3$ was decreased to 0.30 ns. The shortened lifetime of the sensing probe in presence of alcohol indicates the dynamic quenching behavior. The H-bonding interaction takes place between CTAB@CsPbBr$_3$ and alcohols might trigger some non-radiative decay. When the analyte alcohol is added, the interaction the H-bonding interaction between the alcohol molecule with the bromide ions can pull Br$^-$ ion from the perovskite surface. Similarly, with the addition of ethanol, the detachment of cetyl tetra-butyl ammonium cations compete with the ammonium ions to interact with the surface. Thus, the ammonium ion and the Br$^-$ detachment results in the formation of some cation and anion vacancies and creates some charge recombination and hence, quenching of fluorescence of the emission at 550 nm.
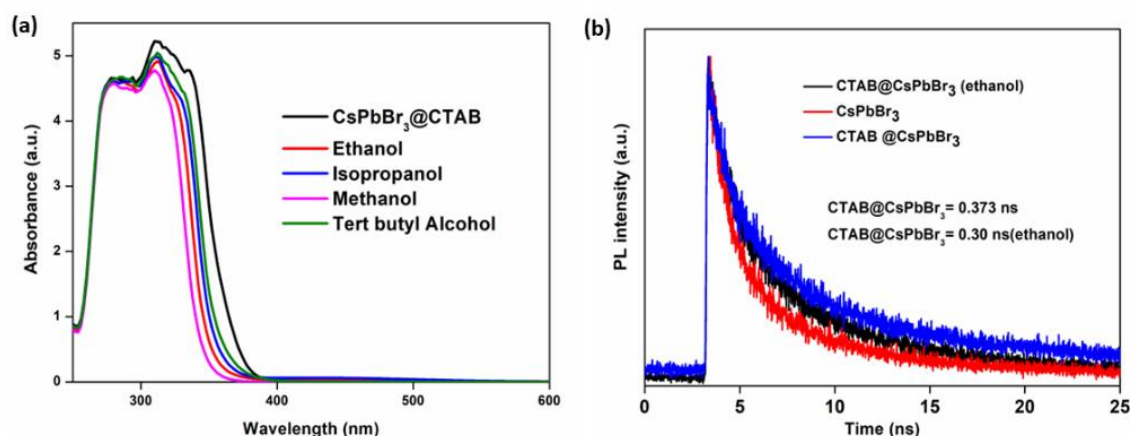
Figure 3.20 (a) UV-Vis absorbance spectra of CTAB@CsPbBr$_3$ upon addition of alcohols, (b) TRPL decay graphs of CTAB@CsPbBr$_3$ before and after exposure to alcohols

However, the fluorescence turn-on response ability at the wavelength of 430 nm might be due to the degradation of CTAB@CsPbBr$_3$ to PbBr$_2$ in presence of ethanol. As illustrated the previous discussion in figure 3.14(a); the intensity of the emission peak at 530 nm showed a gradual increment with the gradual addition of ethanol which is attributed due to the increase in the concentration of the PbBr$_2$. The degradation of CTAB@CsPbBr$_3$ to PbBr$_2$ (CsPbBr$_3 \rightarrow$ PbBr$_2$) is selectively eased titration among the other tested alcohols (Figure 3.14 b-c). Further, the XRD spectra of ethanol-exposed CTAB@CsPbBr$_3$ (adding co-solvent toluene) facilitate the emergence of two new peaks at 28° and 39° characteristics of (210) and (031) planes of PbBr$_2$ and this situation was not observed in case of methanol exposure (Figure

3.21a-c). This observation reveals that the mechanism might involve both dynamic and static processes. The response time of the sensing process is further evaluated after adding 1.15 ppm of ethanol to the perovskite solution. In figure 3.22b, we have noted that the luminescence intensity decreases rapidly after adding alcohols and becomes stable after 2 min. Hence, the response time of the quenching process is 2 min.
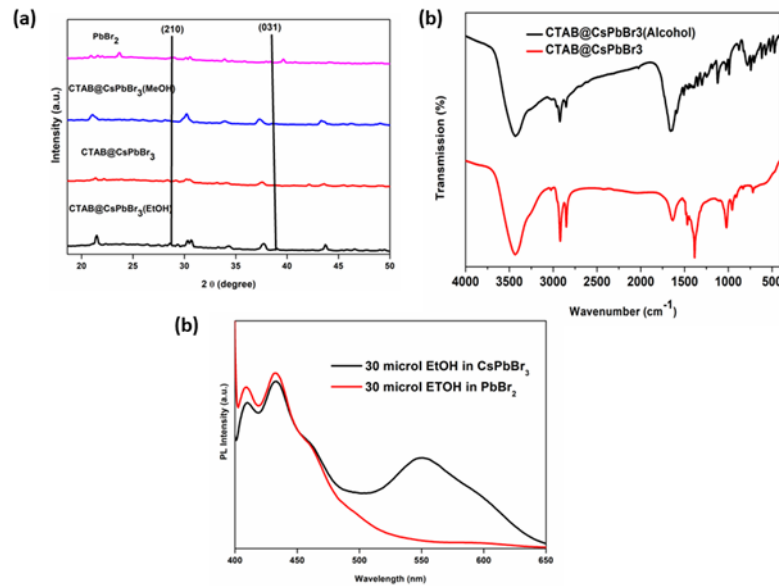
Figure 3.21 (a) XRD spectra of PbBr$_2$ (pink Curve), CTAB@CsPbBr$_3$-MeOH (blue curve), CTAB@CsPbBr$_3$ (red Curve), CTAB@CsPbBr$_3$-EtOH (black Curve), (b) FT-IR graph of CTAB@CsPbBr$_3$ before and after exposure to ethanol, and (c) fluorescence spectra graph of CsPbBr$_3$ and PbBr$_2$ in DMF solution upon 310 nm excitation
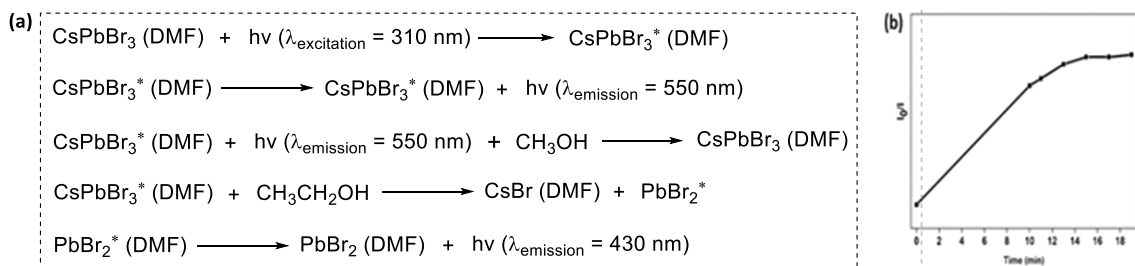

Figure 3.22 (a) Schematic representation of the processes involved in the sensing process, (b) response time measurement of CTAB@CsPbBr$_3$ towards ethanol sensing

3.4 Validation of the proposed sensor using real samples

To evaluate the solution phase sensing performance of CTAB@CsPbBr$_3$ towards ethanol, the sensing method was checked in real samples assays such as ethanol

blending percentage in petrol collected from different sources and cough syrup samples (Figure 3.23 and 3.24). The results exhibited that the addition of petrol to the CTAB@CsPbBr$_3$ in DMF solution decreased the emission signal at 550 nm as well as the emergence of the peak at 430 nm. The limit of detection calculated from the calibration curve fitting was 7.3 ppb. The estimated amount of ethanol in the petrol sample was found as 5% (Figure 3.23a). The obsevation indicates the reliability and accuracy to detect and quantify of ethanol in real samples.
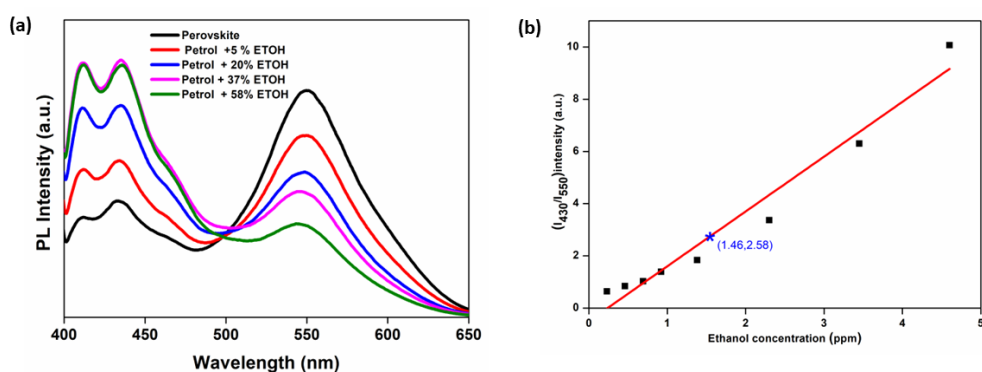
Figure 3.23 Calibration curve for quantification of ethanol in ethanol blended petrol
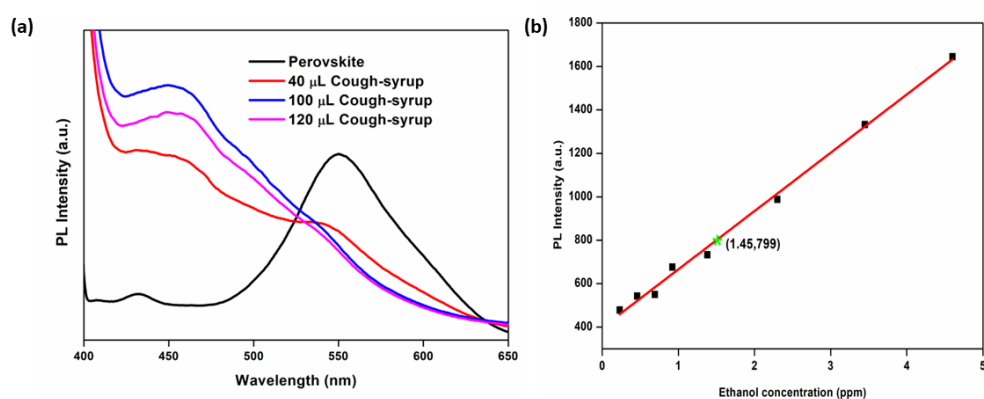
Figure 3.24 Calibration curve for quantification of ethanol in cough-syrup

Table 3.4 Determination of ethanol in blended petrol and cough-syrup samples using CTAB@ CsPbBr$_3$.

	Added (ppm)	Found (ppm)	Recovery %	RSD %
Ethanol blended petrol	1	0.94	94	3.4
Cough - Syrup	1.45	1.5	103	2.2

3.5 Conclusion

The effect of different ionic and non-ionic surfactants on the fluorescence behaviour of $CsPbBr_3$ was studied. This chapter discussed that $CTAB@CsPbBr_3$ was used as an optical sensor for the detection of alcohol owing to its higher stabilities compared to other surfactants. Moreover, $CTAB@CsPbBr_3$ enabled to discriminate ethanols from other alcohols based on their different mode of interaction. Ethanol induced fluorescence turn-on at 430 nm region while other alcohols gave a turn-off response of 550 nm emission of $CTAB@CsPbBr_3$. The emission peak at 550 nm can be used to detect alcohols from other laboratory-used solvents and the emission peak at 430 nm can able to detect ethanol from other alcohols. The efficiancy of the sensor was further validated by measuring ethanol in ethanol-blended petrol and cough syrups. The limit of detection of the calculated quenching process was 7.3 ppb with a fast response of 2 min.

3.6 Bibliography

[1] Ossowicz, P., Klebeko, J., Janus, E., Nowak, A., Duchnik, W., Kucharski, L., and Klimowicz, A. The effect of alcohols as vehicles on the percutaneous absorption and skin retention of ibuprofen modified with *L*-valine alkyl esters. *RSC Advances*, 10(68):41727-41740, 2020.

[2] Sarp, S., Hernandez, S. G., Chen, C., and Sheehan, S. W. Alcohol production from carbon dioxide: methanol as a fuel and chemical feedstock. *Joule*, 5(1):59-76, 2021.

[3] Tulashie, S. K., Appiah, A. P., Torku, G. D., Darko, A. Y., and Wiredu, A. Determination of methanol and ethanol concentrations in local and foreign alcoholic drinks and food products (Banku, Ga kenkey, Fante kenkey and Hausa koko) in Ghana. *International Journal of Food Contamination*, 4(1):1-5, 2017.

[4] Tseng, K. N. T., Lin, S., Kampf, J. W., and Szymczak, N. K. Upgrading ethanol to 1-butanol with a homogeneous air-stable ruthenium catalyst. *Chemical Communications*, 52(14):2901-2904, 2016.

[5] Barceloux, D. G., Randall Bond, G., Krenzelok, E. P., Cooper, H., and Allister Vale, J. American Academy of Clinical Toxicology practice guidelines on the treatment of methanol poisoning. *Journal of toxicology: Clinical Toxicology*, 40(4):415-446, 2002.

[6] Liu, J. J., Daya, M. R., and Mann, N. C. Methanol-related deaths in Ontario. *Journal of toxicology: Clinical Toxicology*, 37(1):69-73, 1999.

[7] Onder, F., İlker, S., Kansu, T., Tatar, T., and Kural, G. Acute blindness and putaminal necrosis in methanol intoxication. *International Ophthalmology*, 22:81-84, 1999.

[8] Paasma, R., Hovda, K. E., Tikkerberi, A., and Jacobsen, D. Methanol mass poisoning in Estonia: outbreak in 154 patients. *Clinical Toxicology*, 45(2):152-157, 2007.

[9] Chen, L., Yin, S. Y., Pan, M., Wu, K., Wang, H. P., Fan, Y. N., and Su, C. Y. A naked eye colorimetric sensor for alcohol vapor discrimination and amplified spontaneous emission (ASE) from a highly fluorescent excited-state intramolecular proton transfer (ESIPT) molecule. *Journal of Materials Chemistry C*, 4(29):6962-6966, 2016.

[10] Ma, Y., Xiao, J., Zhang, Q., Ma, C., Jiang, X., Wu, B., and Zeng, X. Single-crystal perovskite LaBaCo2O6-δ micro-sensors for gas detection in humid environment. *Journal of Alloys and Compounds*, 801:360-366, 2019.

[11] Jia, X., Fan, H., Lou, X., and Xu, J. Synthesis, and gas sensing properties of perovskite $CdSnO_3$ nanoparticles. *Applied Physics A*, 94:837-841, 2009.

[12] Chen, S. H., Wu, H. L., Yen, C. H., Wu, S. M., Lin, S. J., and Kou, H. S. Trace determination of methanol in water–ethanol solution by derivatization and

high-performance liquid chromatography. *Journal of Chromatography A*, 799(1-2):93-99, 1998.

[13] Pérez-Ponce, A. and Garrigues, S. Vapour phase Fourier transform infrared spectrometric determination of carbonate in sediments. *Analyst*, 123(9):1817-1821, 1998.

[14] Allen, T. M., Falconer, T. M., Cisper, M. E., Borgerding, A. J., and Wilkerson, C. W. Real-time analysis of methanol in air and water by membrane introduction mass spectrometry. *Analytical Chemistry*, 73(20):4830-4835, 2001.

[15] Han, T., Yang, J., Miao, R., Liu, K., Li, J., Wang, D., Liu, T., and Fang, Y. Direct Distinguishing of Methanol over Ethanol with a Nanofilm-Based Fluorescent Sensor. *Advanced Materials Technologies*, 6(2):2000933, 2021.

[16] Liu, S., Liu, X., Gong, Y., Hu, Q., and Yu, L. π-Electronic Coassembled Microflake Sensors with Förster Resonance Energy Transfer Enhanced Discrimination of Methanol and Ethanol. *ACS Applied Materials & Interfaces*, 14(11):13980-13988, 2022.

[17] Li, D. Y., Song, J. H., Cheng, Y., Wu, X. M., Wang, Y. Y., Sun, C. J., Yue, C. Y., and Lei, X. W. Ultra-Sensitive, Selective and Repeatable Fluorescence Sensor for Methanol Based on a Highly Emissive 0D Hybrid Lead-Free Perovskite. *Angewandte Chemie International Edition*, 134(35):e202206437, 2022.

[18] Shen, T., Tan, D., Shanmugham, M., and Liu, X. Rapid quantification of ethanol content in aqueous solutions using a ratiometric fluorescent sensor. *Sensors & Diagnostics*, 1(4):714-718, 2022.

[19] Chen, B., Li, L., Hu, Y., Liu, B., Guo, M., Zhang, Q., Yang, Q., and Zhang, M. Fluorescence turn-on immunoassay of endocrine diethyl phthalate in daily supplies using red fluorescent carbon dots. *Microchemical Journal*, 178:107350, 2022.

[20] Liu, D., Kumar, R., Wei, F., Han, W., Mallik, A. K., Yuan, J., Wan, S., He, X., Kang, Z., and Li, F. High sensitivity optical fiber sensors for simultaneous measurement of methanol and ethanol. *Sensors and Actuators B: Chemical*, 271:1-8, 2018.

[21] Wu, D., Sedgwick, A. C., Gunnlaugsson, T., Akkaya, E. U., Yoon, J., and James, T. D. Fluorescent chemosensors: the past, present, and future. *Chemical Society Reviews*, 46(23):7105-7123, 2017.

[22] Afaneh, A. T. and Schreckenbach, G. Fluorescence enhancement/quenching based on metal orbital control: computational studies of a 6-thienyllumazine-based mercury sensor. *The Journal of Physical Chemistry A*, 119(29):8106-8116, 2015.

[23] Aamir, M., Sher, M., Malik, M. A., Akhtar, J., and Revaprasadu, N. A chemodosimetric approach for the selective detection of Pb^{2+} ions using a cesium-based perovskite. *New Journal of Chemistry*, 40(11):9719-9724, 2016.

[24] Casanova-Chafer, J., Garcia-Aboal, R., Atienzar, P., and Llobet, E. The role of anions and cations in the gas sensing mechanisms of graphene decorated with lead halide perovskite nanocrystals. *Chemical Communications*, 56(63):8956-8959, 2020.

[25] Wei, Y., Xu, Y., Wang, Q., Wang, J., Lu, H., and Zhu, J. $CsPbBr_3$ nanowire polarized light-emitting diodes through mechanical rubbing. *Chemical Communications*, 56(40):5413-5416, 2020.

[26] Xiang, X., Ouyang, H., Li, J., and Fu, Z. Humidity-sensitive $CsPbBr_3$ perovskite based photoluminescent sensor for detecting water content in herbal medicines. *Sensors and Actuators B: Chemical*, 346:130547, 2021.

[27] Yang, N., Wen, Q. L., Fu, Y. B., Long, L. F., Liao, Y. J., Hou, S. B., Qian, P., Liu, P., Ling, J., and Cao, Q. A lead-free Cs_2ZnCl_4 perovskite nanocrystals fluorescent probe for highly selective detection of norfloxacin. *Spectrochimica Acta Part A: Molecular and Biomolecular Spectroscopy*, 281:121568, 2022.

[28] Jan, Q., Nabi, S., Sofi, F. A., and Bhat, M. A. $CsPbBr_3$ perovskite nanoplatelets: Excellent probes for spectrofluorimetric sensing of chloride and arsenite. *Spectrochimica Acta Part A: Molecular and Biomolecular Spectroscopy*, 270:120749, 2022.

[29] Chen, C., Cai, Q., Luo, F., Dong, N., Guo, L., Qiu, B., and Lin, Z. Sensitive fluorescent sensor for hydrogen sulfide in rat brain micro-dialysis *via* $CsPbBr_3$ quantum dots. *Analytical Chemistry*, 91(24):15915-15921, 2019.

[30] Feng, X., Zhang, X., Huang, J., Wu, R., Leng, Y., and Chen, Z. $CsPbBr_3$ and $CsPbBr_3/SiO_2$ Nanocrystals as a Fluorescence Sensing Platform for High-Throughput Identification of Multiple Thiophene Sulfides. *Analytical Chemistry*, 94(15):5946-5952, 2022.

[31] Tan, L., Guo, M., Tan, J., Geng, Y., Huang, S., Tang, Y., Su, C., Lin, C., and Liang, Y. Development of high-luminescence perovskite quantum dots coated with molecularly imprinted polymers for pesticide detection by slowly hydrolyzing the organosilicon monomers in situ. *Sensors and Actuators B: Chemical*, 291:226-234, 2019.

[32] Liu, K., Liang, Q., Qin, M., Shen, D., Yin, H., Ren, Z., Zhang, Y., Zhang, H., Fong, P. W., and Wu, Z. Zwitterionic-surfactant-assisted room-temperature coating of efficient perovskite solar cells. *Joule*, 4(11):2404-2425, 2020.

[33] Zhang, L., Lin, H., Wang, C., Liu, W. R., Li, S., Cheng, Y., Xu, J., Gao, H., Li, K. and Copner, N. A solid-state colorimetric fluorescence Pb^{2+} sensing scheme: mechanically driven $CsPbBr_3$ nano-crystallization in glass. *Nanoscale*, 12(16):8801-8808, 2020.

[34] Lu, L. Q., Ma, M. Y., Tan, T., Tian, X. K., Zhou, Z. X., Yang, C., and Li, Y. Novel dual ligands capped perovskite quantum dots for fluoride detection. *Sensors and Actuators B: Chemical*, 270:291-297, 2018.

[35] Liu, L., Wang, Y., Lin, R., Yao, Z., Lin, Q., Wang, L., Zhang, Z., and Xiang, S. Two water-stable lanthanide metal–organic frameworks with oxygen-rich channels for fluorescence sensing of Fe(III) ions in aqueous solution. *Dalton Transactions*, 47(45):16190-16196, 2018.

[36] Zhang, M., Tian, Z. Q., Zhu, D. L., He, H., Guo, S. W., Chen, Z. L., and Pang, D. W. Stable $CsPbBr_3$ perovskite quantum dots with high fluorescence quantum yields. *New Journal of Chemistry*, 42(12):9496-9500, 2018.

[37] Wu, H., Zhang, Y., Lu, M., Zhang, X., Sun, C., Zhang, T., Colvin, V. L., and William, W. Y. Surface ligand modification of cesium lead bromide nanocrystals for improved light-emitting performance. *Nanoscale*, 10(9):4173-4178, 2018.

[38] Huang, H., Yuan, H., Janssen, K. P., Solis-Fernandez, G., Wang, Y., Tan, C. Y., Jonckheere, D., Debroye, E., Long, J., and Hendrix, J. Efficient and selective photocatalytic oxidation of benzylic alcohols with hybrid organic–inorganic perovskite materials. *ACS Energy Letters*, 3(4):755-759, 2018.

[39] Wang, S., Bi, C., Yuan, J., Zhang, L., and Tian, J. Original core–shell structure of cubic $CsPbBr_3$@amorphous $CsPbBr_3$ perovskite quantum dots with a high blue photoluminescence quantum yield of over 80%. *ACS Energy Letters*, 3(1):245-251, 2017.

[40] Guan, Z., Chen, F., Liu, Z., L, P., Chen, M., Guo, M., Li, X., Teng, F., Chen, S., and Tang, A. Compositional engineering of multi-nary Cu–In–Zn-based semiconductor nanocrystals for efficient and solution-processed red-emitting quantum-dot light-emitting diodes. *Organic Electronics*, 74:46-51, 2019.

[41] Brouwer, A. M. Standards for photoluminescence quantum yield measurements in solution (IUPAC Technical Report). *Pure and Applied Chemistry*, 83(12):2213-2228, 2011.

[42] Wu, X., Niu, Q., Li, T., Cui, Y., and Zhang, S. A highly sensitive, selective and turn-off fluorescent sensor based on phenylamine-oligothiophene derivative for rapid detection of Hg^{2+}. *Journal of Luminescence*, 175:182-186, 2016.

[43] Karmakar, R., Neogi, S., Banerjee, A., and Bandyopadhyay, S. Structural; morphological; optical and magnetic properties of Mn doped ferromagnetic ZnO thin film. *Applied Surface Science*, 263:671-677, 2012.

[44] Liu, L., Xu, K., Allen, A. L., Li, X., Xia, H., Peng, L., and Zhang, J. Z. Enhancing the Photoluminescence and Stability of Methylammonium Lead Halide Perovskite Nanocrystals with Phenylalanine. *The Journal of Physical Chemistry C*, 125(4):2793-2801, 2021.

[45] Viana, R. B., da Silva, A. B., and Pimentel, A. S. Infrared spectroscopy of anionic, cationic, and zwitterionic surfactants. *Advances in Physical Chemistry*, 2012, 2012.

[46] Wu, X., Liu, J., Wu, D., Zhao, Y., Shi, X., Wang, J., Huang, S., and He, G. Highly conductive and uniform graphene oxide modified PEDOT: PSS electrodes for ITO-Free organic light emitting diodes. *Journal of Materials Chemistry C*, 2(20):4044-4050, 2014.

[47] Cai, Y., Wang, L., Zhou, T., Zheng, P., Li, Y., and Xie, R. J. Improved stability of $CsPbBr_3$ perovskite quantum dots achieved by suppressing interligand proton transfer and applying a polystyrene coating. *Nanoscale*, 10(45):21441-21450, 2018.

[48] Nithiyanantham, U., Ede, S. R., Ozaydin, M. F., Liang, H., Rathishkumar, A., and Kundu, S. Low temperature, shape-selective formation of Sb_2Te_3 nanomaterials and their thermoelectric applications. *RSC Advances*, 5(109):89621-89634, 2015.

[49] Nandiyanto, A. B. D., Oktiani, R., and Ragadhita, R. How to read and interpret FT-IR spectroscope of organic material. *Indonesian Journal of Science and Technology*, 4(1):97-118, 2019.

[50] Siddiqui, N., Bhardwaj, A., Shaikh, A., Jain, A., and Verma, S. K. Effect of silver loading on optical and antibacterial behaviour of poly(methyl methacrylate). *Oriental Journal of Chemistry*, 30(4):1777-1783, 2014.

[51] Zhang, M., Zheng, Z., Fu, Q., Chen, Z., He, J., Zhang, S., Yan, L., Hu, Y., and Luo, W. Growth, and characterization of all-inorganic lead halide perovskite semiconductor $CsPbBr_3$ single crystals. *CrystEngComm*, 19(45):6797-6803, 2017.